Rigid Airborne docking between a fixed-wing UAV and an over-actuated multicopter

J.J.E. Laffita van den Hove*, E.J.J. Smeur, and B.D.W. Remes
Delft University of Technology, Faculty of Aerospace Engineering, Kluyverweg 1, Delft, Zuid-Holland, The Netherlands

ABSTRACT

Fixed-wing aircraft fly longer, faster, and further than rotorcraft, but cannot take off or land vertically. Hybrid drones combine VTOL with a wing for forward flight, but the hovering system generally makes them less efficient than a pure fixed-wing. We propose an alternative, in which a rotorcraft is used to assist the fixed-wing UAV with the VTOL portions of the flight. This paper takes the first steps towards this alternative by developing and testing an overactuated rotorcraft that can autonomously dock onto a target at fixed-wing velocities. The control system uses Incremental Non-Linear Dynamic Inversion Control (INDI) to achieve linear accelerations with lateral and longitudinal motors, enabling robust horizontal control independent of attitude. A relative guidance algorithm for the docking approach path is presented, along with a vision sensing approach using ArUco markers and IR LEDs. Successful docking and separation were achieved in the wind tunnel at speeds of up to 15m/s.

1 INTRODUCTION

Unmanned aerial vehicles have seen a rapid increase in use and development over the last decade[1]. For most uses, it is more common to use rotorcraft as opposed to fixed-wing aircraft, due to their capability of vertical takeoff and landing (VTOL) as well as hovering. While the need to hover may be a pre-requisite for some missions, it is not a requirement for all of them. Of course being able to takeoff and land vertically is beneficial, but it comes at the cost of flight endurance and range[2].

Hybrid UAVs combine VTOL capability with a wing for efficient forward flight, but they tend to be harder to control during hovering, due to the wing surface that can catch gusts, and they are less efficient during cruise flight due to the extra systems needed to facilitate hovering. That is where the need for airborne docking comes in. A rotorcraft could be used to assist in the takeoff and landing of the fixed-wing aircraft, such that the fixed-wing can be optimized for efficient flight while retaining the VTOL capability. The authors propose the use of an overactuated rotorcraft with electromagnets as the docking solution.

1.1 Relevant work

Airborne docking systems can be categorized as rigid or non-rigid, the former being systems for which the docking apparatus is comprised of rigid members while the latter utilizes flexible materials that can easily deform such as ropes or nets.

Various non-rigid docking solutions have been developed to recover fixed-wing UAVs without a landing strip. One approach involves arresting systems using horizontal or vertical ropes in combination with a hooking mechanism at the tail or wingtips [3, 4, 5]. This can be achieved using a multicopter, a crane, or a kite dragged by a moving vehicle. Although these approaches require infrastructure and manual recovery, the control of the fixed-wing does not need to be very precise in order to attach to the rope.

A completely airborne variation of the aforementioned solution is presented in [6], where two multicopters are used to carry the arresting rope. The rotorcrafts used RTK GPS to position themselves in the right position for successful capture. The fixed-wing has a line with a hook attached to it, which it uses to hook onto the horizontal catch line held by the rotorcrafts. The recovery margins are dictated by the length of the hook line and horizontal catch line, which can potentially be increased. A similar method was used with a net in [7], which was experimentally verified [8]. However, the net method had drawbacks including increased weight and wind influence, as well as a higher risk of equipment damage compared to single hook alternatives.

Current systems that would allow for docking and separation mid-flight have been in the form of a probe and drogue approach. Extensive research has gone into Air-to-Air refueling for large aircraft, which is summarized in [9]. In the world of smaller UAVs, Wilson successfully had a fixed-wing UAV to autonomously dock with a drogue towed by another UAV[10]. To improve the estimation of the relative distance between the UAVs, his system fuses direct vehicle-to-vehicle observations in the state estimates. Dynetics successfully recovered an X-61A aircraft using a drogue towed from a C130 Aircraft[11].

With regards to rigid solutions, Steven Lukow aimed to design and fabricate a prototype of an autonomous multirotor drone that can dock onto a larger fixed-wing drone for Mars exploration [12]. Electromagnetic coils mounted on the

*Email address(es): jonathaslvdh@gmail.com

fixed-wing drone were used to form a connection with two neodymium magnets mounted on the top of the multirotor. A demonstration was not shown. In [13] the author uses a marker on an unmanned ground vehicle (UGV), such that a fixed-wing UAV could recognize the target and relative pose, and finally land on it. Tests were done at very slow speeds, and the system became unstable at higher speeds. In [14] the same setup is used, but this time with a gimballed camera that points towards the received location of the ground vehicle. Successful landings were achieved on a high-speed ground vehicle traveling at 50km/h.

Clearly, there have been many advancements toward airborne docking. However, there is no instance of it being done between rotorcraft and a fixed-wing UAV at forward flight velocities.

1.2 Contributions

The airborne docking concept proposed involves an overactuated multicopter that approaches a fixed-wing aircraft from below to avoid disturbing the airflow over the aircraft's aerodynamic surfaces and dock onto it rigidly using electromagnets. To achieve the precise relative control desired for the docking maneuver, three additional motors are added to the multicopter: two laterally and one longitudinally. This also allows to decouple position from attitude.

This paper focuses on the rotorcraft, and the contributions are as follows. A relative control and guidance strategy for the overactuated platform is put forward, and validated by performing wind tunnel experiments at fixed-wing velocities with a static target. The use of electromagnets as a docking system is also put to the test. A relative sensing method that uses IR LEDs in combination with retroreflective ArUco markers are used. An illustration of the system can be seen in Figure 1.

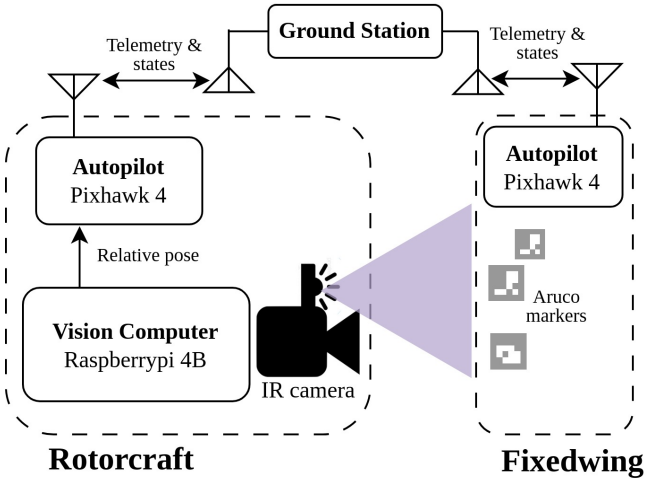

Figure 1: System Architecture.

2 CONTROL

2.1 INDI for linear accelerations

Traditional rotorcraft need to adjust the attitude in order to control their position. This is identified as a potential problem in the docking process. To be able to control the position of the rotorcraft independently of attitude, one back propeller and two side propellers are used, resulting in an over-actuated platform, as can be seen in Figure 2. To simplify the control problem, the four propellers facing downward are used for attitude control and the generation of vertical lift, while the 3 side propellers are used for horizontal position control. The attitude of the drone is controlled with INDI [15]. It is assumed that the moments resulting from the lateral-acting motors are negligible, and any effect they do have will be treated as a disturbance. For position control, a variation of [16] is be implemented, where the side actuation is used instead of the attitude angle to achieve horizontal control. The two reference frames that are used in this section are the body frame and the North, East Down (NED) frame, which is assumed to be an inertial frame. The body frame is depicted in Figure 2 and is denoted by subscript B. The NED frame, indicated with subscript N, has its axes pointing North, East, and Down, and its origin is fixed to a point on earth of choice.

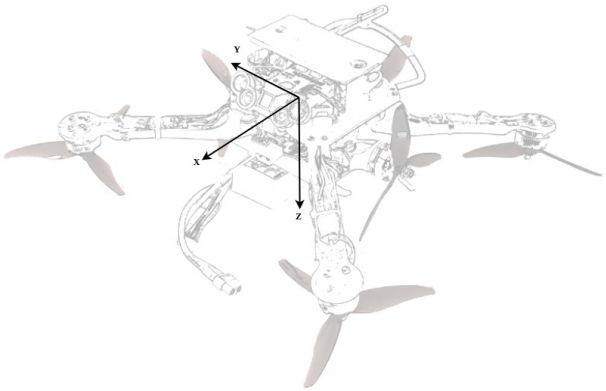

Figure 2: Body reference Frame.

The position dynamics of the aircraft in the NED frame is given by Newton's second law of motion:

$$\ddot{\xi} = g + \frac{1}{m}F(\dot{\xi}, w) + \frac{1}{m}T_N(\eta, T_B), \tag{1}$$

where ξ is the position of the vehicle, g is the gravity vector, F is the sum of aerodynamic forces acting on the airframe, and T is the thrust vector, which contrary to other conventional multicopters does not only act through the z-axis of the vehicle.

The aerodynamic force is a function of aircraft velocity $\dot{\xi}$ and wind vector w, and the thrust vector is dependent on the attitude of the drone $\eta = \begin{bmatrix}\phi & \theta & \psi\end{bmatrix}^T$, expressed in Euler angles with the traditional ZYX rotation order, as well as the

total thrust T_B in the body frame. Due to the side motors, the vehicle can produce thrust along all axes, as opposed to only along the Z axis. T_N is given by:

$$\begin{aligned} T_N(\eta, T_B) &= M_{NB}(\eta) T_B \\ &= \begin{bmatrix} c\psi c\theta & c\psi s\theta s\phi - s\psi s\phi & s\psi s\theta + c\phi s\theta c\phi \\ s\psi c\theta & c\psi s\theta s\phi & s\psi s\theta c\phi - c\psi s\phi \\ -s\theta & c\theta s\phi & c\theta c\phi \end{bmatrix} \cdot \begin{bmatrix} T_{B_X} \\ T_{B_Y} \\ T_{B_Z} \end{bmatrix} , \end{aligned} \quad (2)$$

where the sine and cosine are abbreviated by the letters s and c respectively. Now a first order Tailor expansion can be done on Equation 1 to obtain Equation 3:

$$\begin{aligned} \ddot{\xi} &= g + \tfrac{1}{m} F(\dot{\xi_0}, w_0) + \tfrac{1}{m} T_N(\eta_0, T_{B_0}) \\ &+ \tfrac{\sigma}{\sigma \dot{\xi}} \tfrac{1}{m} F(\dot{\xi}, w_0)|_{\dot{\xi}=\dot{\xi}_0} (\dot{\xi} - \dot{\xi}_0) \\ &+ \tfrac{\sigma}{\sigma w} \tfrac{1}{m} F(\dot{\xi}_0, w)|_{w=w_0} (w - w_0) \\ &+ \tfrac{\sigma}{\sigma \phi} \tfrac{1}{m} T_N(\phi, \theta_0, \psi_0, T_{BX_0}, T_{BY_0}, T_{BZ_0})|_{\phi=\phi_0} (\phi - \phi_0) \\ &+ \tfrac{\sigma}{\sigma \theta} \tfrac{1}{m} T_N(\phi_0, \theta, \psi_0, T_{BX_0}, T_{BY_0}, T_{BZ_0})|_{\theta=\theta_0} (\theta - \theta_0) \\ &+ \tfrac{\sigma}{\sigma \psi} \tfrac{1}{m} T_N(\phi_0, \theta_0, \psi, T_{BX_0}, T_{BY_0}, T_{BZ_0})|_{\psi=\psi_0} (\psi - \psi_0) \\ &+ \tfrac{\sigma}{\sigma T_{BX}} \tfrac{1}{m} T_N(\phi_0, \theta_0, \psi_0, T_{BX}, T_{BY_0}, T_{BZ_0})|_{T_{BX}=T_{BX_0}} (T_{BX} - T_{BX_0}) \\ &+ \tfrac{\sigma}{\sigma T_{BY}} \tfrac{1}{m} T_N(\phi_0, \theta_0, \psi_0, T_{BX_0}, T_{BY}, T_{BZ_0})|_{T_{BY}=T_{BY_0}} (T_{BY} - T_{BY_0}) \\ &+ \tfrac{\sigma}{\sigma T_{BZ}} \tfrac{1}{m} T_N(\phi_0, \theta_0, \psi_0, T_{BX_0}, T_{BY_0}, T_{BZ})|_{T_{BZ}=T_{BZ_0}} (T_{BZ} - T_{BZ_0}) \end{aligned} \quad (3)$$

The first terms $g + \frac{1}{m} F(\dot{\xi_0}, w_0) + \frac{1}{m} T_N(\eta_0, T_{B_0})$ can be simplified to the acceleration at the previous time step. This can be obtained by using the IMU acceleration readings and rotating them to the NED frame. The gravitational acceleration must then be added to that. There is no good estimate for the partial derivatives of $F(\dot{\xi}, w)$ as developing an aerodynamic model would be very time-consuming and the changes in the wind are hard to obtain. These two terms will therefore be taken as 0. This does not mean these forces are neglected, as they are included in the term $\ddot{\xi_0}$. The partial derivatives of ϕ, θ, and ψ will also be neglected, as for the time being, there will not be any aggressive attitude commands in the airborne docking maneuver. Implementation of these terms is considered future work.

Equation 3 can now be rewritten into:

$$\ddot{\xi} = \ddot{\xi_0} + \frac{1}{m} G(\eta_0)(u - u_0) , \quad (4)$$

where $\mathbf{u} = [T_{BX} \quad T_{BY} \quad T_{BZ}]$ and

$$G(\eta_0, T_{B0}) = R_{NB} \cdot \begin{bmatrix} \frac{dT_{BX}}{dT_{BX_c}} \\ \frac{dT_{BY}}{dT_{BY_c}} \\ \frac{dT_{BZ}}{dT_{BZ_c}} \end{bmatrix} , \quad (5)$$

which is referred to as the control effectiveness matrix.

The accelerometer measurements obtained to determine $\ddot{\xi_0}$ are normally very noisy due to vibrations stemming from the rotating propellers. They are therefore filtered using a second order low pass filter. Since a filter introduces a delay, all other terms with subscript 0 must therefore also be filtered with the same filter. Now Equation 4 can be inverted to obtain:

$$u_c = u_f + mG^{-1}(\eta_0)(v_{\ddot{\xi}} - \ddot{\xi}_f). \quad (6)$$

Note that all values that are filtered are denoted with a subscript f. The virtual control $v_{\ddot{\xi}}$ is the desired acceleration of the vehicle and u_c is the resulting control output. The control block diagram can be seen in Figure 3.

2.1.1 Thrust estimation

The actuator dynamics can be modeled using the 1st order system shown in Equation 7

$$A(z) = \frac{\alpha}{z - (1 - \alpha)} \quad (7)$$

where α was estimated to be 0.069 at 500Hz.

The vertical control increment $\widetilde{T}_{BZ}$ is controlled through the four down-facing propellers and is passed to the inner attitude loop. The way this thrust increment is used is further described in [15]. Since the over-actuated multicopter is designed to be flying forward at fixed-wing aircraft speeds, there will always be an aerodynamic force acting in the negative X_B direction. One motor acting forwards is therefore sufficient for longitudinal control. At lower speeds, where aerodynamic drag is not significant for longitudinal control, the two aircraft are already docked, so precise control is not needed. In this case, reversing the direction of rotation of the propeller is sufficient for longitudinal control, albeit using different gains due to the slower dynamics. For lateral control, two motors facing away from each other are used. The PWM command to each lateral motor is:

$$T_{L_c} = T_{min} \leq T_{base} + T_{BY_c} \leq T_{max} , \quad (8)$$

$$T_{R_c} = T_{min} \leq T_{base} - T_{BY_c} \leq T_{max} \quad (9)$$

Where T_{L_c} and T_{R_c} are the command to the left and right motor respectively, T_{base} is the baseline thrust of both motors and T_{BY_c} is the commanded side thrust. The total side thrust T_{B_Y} then results from subtracting the thrust of the left and right motor.

A quadratic relationship governs the rotational speed of the propellers and thrust. That means that the thrust effectiveness ($\frac{dT}{dT_c}$) of each motor increases linearly with its rotational speed. In the context of the side propellers, increasing T_{BY_c} will lead to an increase in the thrust effectiveness of the left motor. However, it will also lead to an equal decrease in the thrust effectiveness of the right motor. The overall effectiveness of the lateral command $\frac{dT_{BY}}{dT_{BY_c}}$ will therefore remain constant as long as $T_{BY_c} \leq min(T_{base} - T_{min}, T_{max} - T_{base})$. Beyond that, only the thrust effectiveness of the unsaturated motor will change, so the assumption that the total effectiveness of both motors remains constant does not hold anymore. It will then change linearly for higher lateral commands.

For the longitudinal thrust, the control effectiveness of the pusher motor was determined at an airspeed of $12m/s$. Since the effectiveness changes with the propeller RPM, flying at higher or lower speeds tends to give an oscillatory response.

In Figure 4, we can appreciate the vehicle response to lateral acceleration commands at various roll angles. The acceleration is tracked well, except for when saturation occurs due

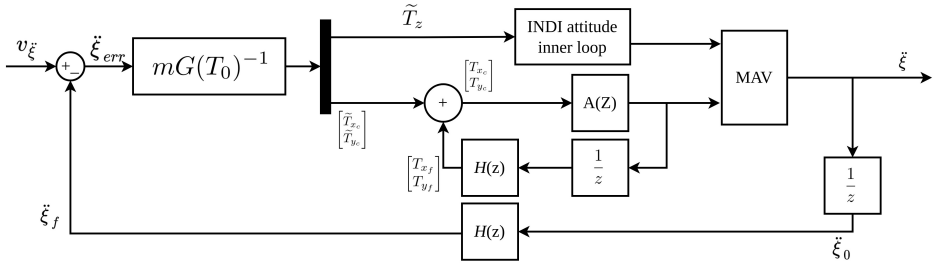

Figure 3: Control diagram of the guidance loop

to a large acceleration command in combination with a roll angle.

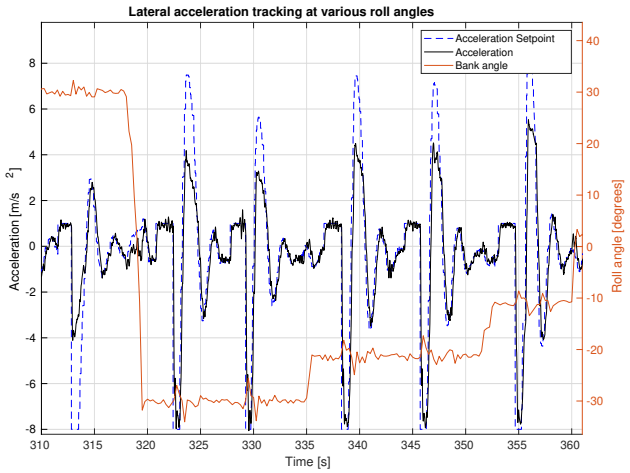

Figure 4: Lateral acceleration tracking at varying roll angles.

2.2 *Position Control*

In subsection 2.1 the way INDI control is used to achieve linear accelerations is put forward. Now position must be controlled by commanding desired accelerations to the INDI controller in the NED frame. To do this, a simple cascaded proportional controller is used and can be observed in Figure 6. The commanded relative velocity is $\dot{\xi}_{ref} = \xi_{ref} \cdot K_p$ and the acceleration $v_{\ddot{\xi}} = \dot{\xi}_{ref} \cdot K_{\dot{\xi}}$.Due to the physical limitations of the aircraft, $\dot{\xi}_{ref}$ and $v_{\ddot{\xi}}$ are bounded to 15m/s and 6m/s^2 respectively. The gains can be tuned such that the response is sufficiently fast, while preventing significant overshoot. In Figure 5 we can see a response to a position step command 2.75m to the right. This was achieved with a velocity gain of 2.0 ms^{-2}/(ms^{-1}) and a position gain of 3.0 ms^{-1}/m.

2.3 *Setpoint generation*

Now that the position of the rotorcraft can be controlled, the setpoint generation to achieve successful docking is considered. Note that the position and velocity errors now become relative errors, but the controller performance should stay unaffected if the fixed-wing drone flies at a constant

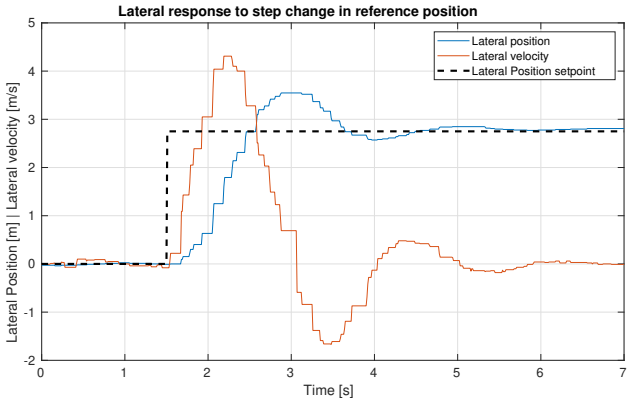

Figure 5: Position response to a step input.

speed. Values will be in the NED frame, with the fixed-wing UAV in the origin. As mentioned before, the rotorcraft must first reach a pre-docked setpoint, after which it starts the approach. This approach path can be visualized in Figure 7. The rotorcraft position reference will advance from the pre-docked position P_{pd} to the docked position P_d gradually until docking is achieved. To ensure that the approach leads to a successful docking attempt, the reference will only advance if the rotorcraft error to its target is within a certain horizontal distance threshold. This threshold is made linearly smaller as the distance to the aircraft is decreased. That is why the two dashed lines seen in Figure 7 get closer to each other. Algorithm 1 shows the approach logic.

The reference position is given by:

$$\xi_{ref} = \xi_{fw} + \begin{bmatrix} \cos\psi_{fw} & -\sin\psi_{fw} & 0 \\ \sin\psi_{fw} & \cos\psi_{fw} & 0 \\ 0 & 0 & 1 \end{bmatrix} \cdot \left(P_{pd} + K_{adv} \cdot (P_d - P_{pd})\right), \tag{10}$$

Where ξ_{fw} is the fixed-wing NED position and K_{adv} is a number from 0 to 1 that dictates, where along the path from P_{pd} to P_d the position reference should be. P_{pd} and P_d are a predetermined position with respect to the aircraft, in which the reference frame is the NED frame rotated along the Z axis by the fixed-wing aircraft heading ψ_{fw}. X therefore points in the same direction as the fixed-wing aircraft, and the point $\begin{bmatrix} 2 & 0 & -5 \end{bmatrix}^T$ is 2 meters below, and 5 meters behind the aircraft. Note that the reference position does not change due to

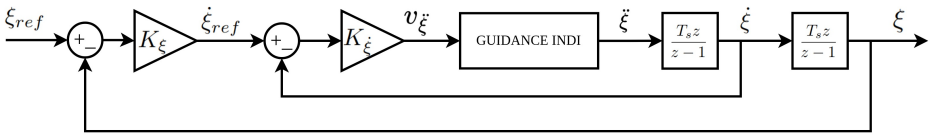

Figure 6: Position control loop

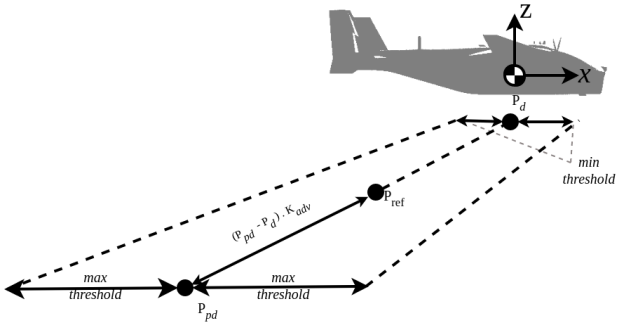

Figure 7: Setpoint generation.

a pitch or roll change of the fixed-wing, but is affected by a change in its heading.

In the docking sequence, the rotorcraft first reaches the *pre-docked* position. Then, the setpoint moves along the approach path towards the *Docked* position. At every iteration of the setpoint generation module (running at 100 Hz), the rotorcraft's horizontal distance to the approach center-line is evaluated, and if it is within the error threshold, then the reference progresses forward. If the aircraft is outside the error threshold, then the reference is moved backward. The amount by which the setpoint progresses along that line is defined by the value k_{adv}.

The error threshold E_{th} is also scaled by k_{adv}, to allow for more error when further away from the fixed-wing. During the experiments, this error threshold decreases linearly from 0.4m at the pre-docked setpoint, to 0.1m at the docked setpoint.

To avoid rapid changes in the reference position due to a momentary change in the heading of the fixed-wing, ψ_{fw} is first filtered with a low pass filter. The commanded heading of the rotorcraft is also set to ψ_{fw}.

2.4 Switching between GPS and vision

To achieve successful docking, the relative position should be accurately estimated. This could be potentially possible with RTK GPS, but in order not to rely on an RTK fix, computer vision is used to augment the GPS. The pre-docked setpoint is, therefore, a point where the two aircraft can be positioned in a safe, yet close enough distance so that the vision system is operative. Once the vision estimates have a good confidence, the relative positioning is done purely on vision. During the approach, vision dropouts can occur. To avoid dropping back to GPS and therefore to the pre-docked setpoint straight away, a buffer is implemented, as can be seen in algorithm 1 where the *Vision confidence* decreases with every loop iteration during a dropout, eventually reaching 0 and forcing the fallback to GPS. While in the dropout, the relative position estimate remains the same, and therefore, the relative acceleration command also remains the same.

```
Input: Detected markers, position estimate (vision & GPS
Output: updated Setpoint
Setpoint ← predocked Setpoint;
while in flight do
    if markers detected > 2 then
        increase vision confidence;
    else
        decrease vision confidence;
    end
    if vision confidence > threshold then
        // Use vision
        if horizontal error < threshold then
            move Setpoint forward;
        else
            move Setpoint backwards;
        end
    else
        // Use GPS
        Setpoint ← predocked Setpoint;
    end
end
```

Algorithm 1: Setpoint generation at module frequency (100hZ)

3 RELATIVE SENSING

To implement the developed control system, the relative position, relative heading, and relative velocity of the two vehicles must be estimated accurately. For the proposed rigid docking apparatus to work the position accuracy must be at least 5cm. To do so, GPS and a monocular camera will be used in cooperation. The GPS measurements, which can achieve a relative position accuracy lower than 2 meters [17], will be used to reach a formation within the range of the vision system. Once within range, the more accurate vision system estimates the relative pose and its derivative to perform the docking maneuver.

3.1 Vision

To estimate the aircraft's relative pose using a monocular camera, a Perspective-N-Point problem is solved using OpenCV. The process involves detecting known points on the aircraft and finding the transformation matrix which minimizes the re-projection error between the 2D image points and the 3D object points. In [18] the authors used the corners of ArUco markers placed on a drone to estimate relative pose. In [10] Wilson used a known pattern of IR LEDs that could

be used as object points and could be detected at a distance of up to $30m$ away.

In this proof of concept, we use a combination of both implementations; ArUco markers will be used for their already-implemented detection algorithms, and the markers are made of IR reflective tape (3M High-Reflex-Tape type 7610). The rotorcraft is equipped with 940nm IR LEDs, and a band-pass filter around the same frequency is used on the camera to minimize any unwanted light. This makes the markers clearly visible in a wide range of lighting conditions.

A comparison between a regular black and white marker and the proposed retroreflective markers is shown in Figure 8. The retroreflective marker offers better visibility and distinct edges, enhancing detection. Selection of the reflective tape is critical to prevent overexposure caused by the IR LEDs. The corner points of the ArUco markers are used as the object points. To ensure marker detection at a range, a combination of small and large ArUco markers is placed around the aircraft. This approach increases the scope of the marker detection [18].

The vision computer used is a RaspberryPi 4B that is constantly running three threads. The first thread processes the camera feed and estimates the relative pose (translation and rotation). The second thread uses the same feed to calculate the optical flow. The third thread sends the estimated relative distance in the body frame, the optical flow, and the relative heading to the autopilot through a serial interface. With this setup, the relative pose is estimated at an average of $32Hz$ at a resolution of 640 x 480 pixels.

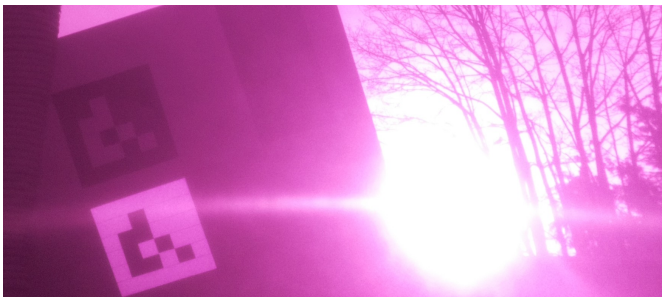

Figure 8: Conventional ArUco marker compared to proposed marker when backlit.

3.2 *Calculating the relative state*

After the visible markers have been detected, the 4 corner points of each of them are known. Given that the marker ID of each of these points are known, and the exact location where these markers are placed on the UAV is also known, we now have a series of (2D) image points with their respective (3D) object points. This data can be directly used in the SolvePnP() function in OpenCV. The estimated translation vector T_{vec} obtained can then be used to find the relative NED position using:

$$\xi_{\text{rel}} = -R_{NB} R_{BC} T_{vec}, \tag{11}$$

where R_{NB} is the rotation matrix from the Body frame to the NED frame, and R_{BC} is the rotation matrix from the camera frame to the body frame, which can be refined by comparing the estimated relative position to the true relative position.

$$\dot{\xi}_{\text{rel}} = \dot{\xi}_{rc} - \dot{\xi}_{fw}, \tag{12}$$

At any point in time, the rotation matrix from the body frame to the NED frame is calculated using the estimated attitude of the rotorcraft. The relative heading ψ_{rel} can be calculated by applying the Rodrigues rotation formula to the obtained rotation vector. The estimated fixed-wing heading ψ_{fw} then becomes:

$$\psi_{fw} = \psi_{rc} + \psi_{rel}\,, \tag{13}$$

where ψ_{rc} is the heading of the rotorcraft. This way, the final approach can take place without communication between the vehicles.

The vision distance estimates are compared with measurements of an external infrared tracking system during several docking attempts. It was observed that the vision error decreases as the aircraft approaches the target. After compensating for camera offset angles, which are seen as constant errors that linearly increased with distance, the absolute error of the vision system is shown in Figure 9. As the rotorcraft approaches the target, the error decreases to below 5cm.

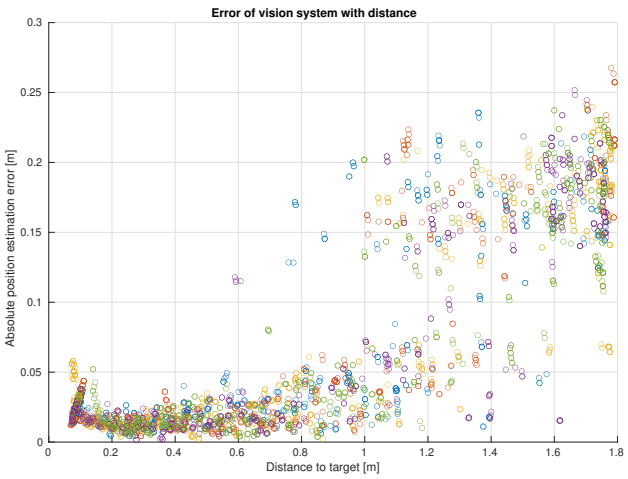

Figure 9: Vision position estimation error with distance.

4 WIND TUNNEL TESTS

As a stepping stone towards outdoor flight, wind tunnel tests were carried out. This allowed us to validate that the over-actuated platform can indeed serve the intended purpose in forward flight, at fixed-wing UAV velocities. The wind tunnel setup allows to keep the follower drone tethered at all times and track its position at mm accuracy, allowing it to be tuned easily, without the risk of crashing.

The facility used is the Open Jet Facility of the TU Delft Aerospace Engineering faculty. It has a cross-section of 2.85m by 2.85m at the test area and can produce wind speeds of up to 30 m/s. The test setup can be seen in Figure 10. To simulate the fixed-wing aircraft, a cruciform beam is attached to the wind-tunnel roof, at the throat, allowing to maximize the approach path size. As can be seen in the image, the follower can be tethered to the roof with a rope and is operated by an assistant in order to always keep the rope slack, without allowing it to get tangled into the propellers. The facility contains a motion capture system called *Optitrack*, which can track position and attitude at mm accuracy and relay it to the UAVs via the ground station.

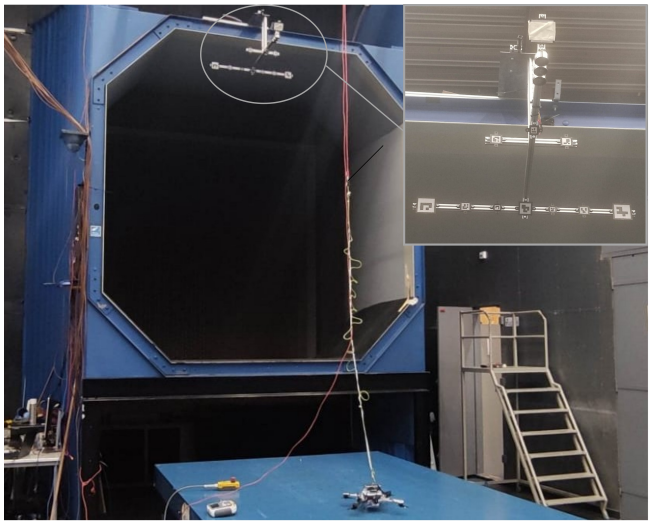

Figure 10: Wind tunnel test setup

4.1 *Fixed-wing aircraft*

The fixed-wing aircraft will be simulated by a cruciform beam and can be seen in Figure 10. Given that most aircraft are of fuselage + wing configuration, that was the shape used. The width and length are both 180mm. Thirteen Aruco markers were placed around the "*airframe*", varying in width, ranging from 2cm to 10cm. This enables the markers to be seen from further away, while still keeping full markers in view when in proximity. Three 25kg pot electromagnets are aligned to form the docking point. In future work, they will be spaced to ensure an exact docking position. The three electromagnets are powered with a 3-cell LiPO battery and can be turned off with a momentary-push button. The electromagnets can therefore be powered off to be able to simulate separation mid-flight.

4.2 *Rotorcraft*

The manufactured rotorcraft can be seen in Figure 2 and its hardware characteristics are tabulated in Table 1. This drone is an adaptation of an F350 drone frame, where the top and bottom plate are re-designed, and 3D printed to accommodate the three lateral motors. A longer landing gear was also made to allow the lateral rotors to spin without hitting the ground. Due to the lateral motors, stronger vibration can now be expected around all three axes. Passive damping is therefore included, where the camera and the flight controller are both suspended on a damped rubber platform.

A flat metal plate is installed that will attach to the electromagnets. A thickness of 3 mm is chosen as it is a good compromise between pull force and mass. Finally, to avoid the tether from getting tangled into the back propeller, a simple propeller guard was included. Note that the four downfacing propellers are in pusher configuration, to assure the necessary clearance for docking.

Table 1: Follower platform characteristics

Take-off weight	1050 [g]
Frame:	Modified F350 plastic drone frame
Motors:	7 x Readytosky 2205 2700kV
ESCs:	Racestar V2 30A
Propellers:	GemFam 5146
Flight controller	Pixhawk 4
On_board computer	Raspberry-pi 4B
Camera	Rasberry-pi v2 noIR
Telemetry	SIK telemetry module
Flight software	Paparazzi

4.3 *Experiment setup and results*

Various tests were carried out to assess the feasibility and discover any challenges of the concept proposed. Three primary questions had to be answered. First, whether the platform can fly at forward velocities matching a fixed-wing aircraft while maintaining level and stable flight. Second, evaluate whether precise enough relative control can be achieved for rigid airborne docking to be feasible. And lastly, verify that the proposed docking method is viable and whether accidental detachments would not take place at these airspeeds.

To answer the first question, the aircraft was flown in the wind tunnel at a fixed position, while airspeed was incrementally increased up to 17.2m/s, at which speed the pusher propeller was saturated. The aircraft remained level with attitude deviations not surpassing 3^o in all axes and its position within 5cm. The relative position tracking capabilities were not affected significantly when flying a flag in front of the aircraft at 14m/s.

The second question is answered by performing the approach and docking procedure in the wind tunnel, starting from the pre-docked position. The aircraft then autonomously approaches the target and docks onto the simulated fixed-wing aircraft. As soon as the operator sees that docking is successful, he turns off the motors and resets the desired position to the pre-docked setpoint. When ready, the operator arms the aircraft and pushes the button that disables the electromagnets. The over-actuated platform then returns to the pre-docked setpoint aggressively. This sequence can be seen

in Figure 11. The security tether is always left slack. Footage of this can be seen on Youtube [1].

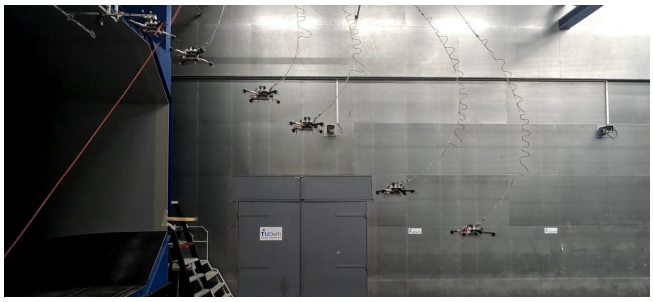

Figure 11: Approach sequence.

The approach path for 5 consecutive docking maneuvers at 13m/s can be seen in Figure 12. The rotorcraft uses Optitrack to reach the pre-docked setpoint, and from there, once the vision confidence is above the threshold, the docking procedure is started with the vision measurements. In these tests, the relative velocity is still obtained from Optitrack. Due to the markers being too small, the pre-docked setpoint had to be moved closer to -1.6m behind and 0.8m below the target. This problem can be mitigated by using larger markers, or increasing the resolution of the camera.

Due to the dimension constraints of the wind tunnel, the approach path is much more horizontal than intended. Because of this, a small deviation in height could lead to the rotorcraft striking the target at the end of the approach. To mitigate this, the final position setpoint is set to be 5cm below the target, and the rotorcraft is given an upward velocity command only if its horizontal position is within 5cm of the target. This resulted in a smooth, continuous docking sequence.

In the figure, the two dark dashed lines are the error threshold around the center line at any given position. This seems like a very narrow approach, but only the horizontal error to the current setpoint is taken into account for the advancement of the desired position setpoint. In fact, we see that the 5 approaches follow almost an identical path that is not through the center line. This is because there is no feedforward control in place to make the rotorcraft exactly track the setpoint, and only the error controller makes the vehicle follow the setpoint, which is advancing faster than what the error controller can keep up with. The follower aircraft is effectively trailing the setpoint by the error threshold. This can be seen in Figure 12, where the rotorcraft (red dot) trails behind the setpoint (blue dot) by the threshold amount (red dashed lines). An animation is also available on Youtube[1]. For this specific scenario, in which the leader is not moving and there is almost no turbulence, it makes the approach very smooth.

[1] https://www.youtube.com/playlist?list=PL_KSX9GOn2P__KdCtqlExlus0Ogasmgbw

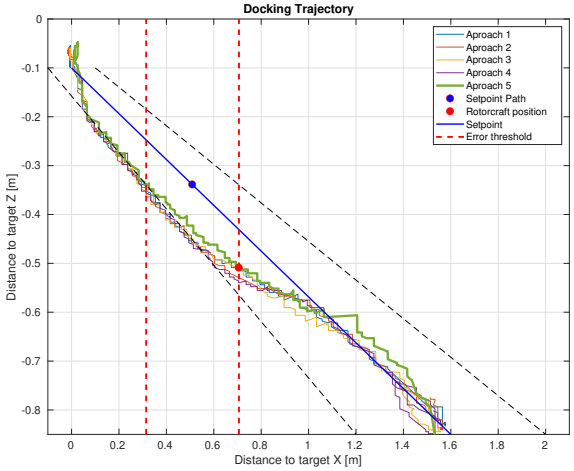

Figure 12: Path for 5 different approaches and setpoint position with respect to AC for the first approach.

4.4 *Additional observations*

While increasing the airspeed gradually from 0 to 15m/s, the aircraft starts oscillating heavily at a forward speed of 5m/s. The oscillations are mainly pitch oscillations, and it seems as if the back propellers are stalling and then recovering. This could be due to interaction between the front and back propellers. Even though the reason for this is still uncertain, it was easily mitigated by avoiding flying at that specific airspeed. In a mission for which this aircraft is designed, constantly flying at 5m/s is not a requirement.

5 CONCLUSIONS & RECOMMENDATIONS

In conclusion, this paper presents a proof of concept for rigid airborne docking using electromagnets between a fixed-wing aircraft and a hybrid rotorcraft. The successful demonstration of autonomous docking and undocking in a wind tunnel environment indicates the potential for future development and outdoor testing. The use of an INDI controller and horizontal motors for handling linear accelerations proved to be very effective and is recommended to be used in future work. The implemented cascaded proportional controller for position control, as well as the setpoint generation method used, yielded a smooth docking maneuver. The relative sensing method employing retroreflective ArUco markers and an infrared camera proved to work well in different lighting conditions. The methods presented in this paper should be tested in an outdoor environment with a real fixed-wing in future work. Overall, this study establishes the feasibility of rigid airborne docking and lays the groundwork for future advancements, holding promise for applications requiring precise docking between fixed-wing and rotorcraft vehicles.

REFERENCES

[1] Nader S Labib, Matthias R Brust, Grégoire Danoy, and Pascal Bouvry. The rise of drones in internet of things: A survey on the evolution,

prospects and challenges of unmanned aerial vehicles. *IEEE Access*, 9:115466–115487, 2021.

[2] Alessandro Bacchini, Enrico Cestino, Benjamin Van Magill, and Dries Verstraete. Impact of lift propeller drag on the performance of evtol lift+ cruise aircraft. *Aerospace Science and Technology*, 109:106429, 2021.

[3] Adarsh Gangwal, Akshika Jain, and Shreeja Mohanta. Blood delivery by drones: A case study on zipline. *International Journal of Innovative Research in Science, Engineering and Technology*, 8(8), 2019.

[4] Hoodtech Mechanical. Flying launch and recovery system. hoodtech-mechanical. https://www.hoodtechmechanical.com/vtol. Accessed: 20-05-2023.

[5] PS Ramesh and JV Muruga Lal Jeyan. Comparative analysis of fixed-wing, rotary-wing and hybrid mini unmanned aircraft systems (uas) from the applications perspective. *INCAS Bulletin*, 14(1):137–151, 2022.

[6] Mads Friis Bornebusch and Tor Arne Johansen. Autonomous recovery of a fixed-wing uav using a line suspended between two multirotor uavs. *IEEE Transactions on Aerospace and Electronic Systems*, 57(1):90–104, 2020.

[7] Kristian Klausen, Jostein Borgen Moe, Jonathan Cornel van den Hoorn, Alojz Gomola, Thor I Fossen, and Tor Arne Johansen. Coordinated control concept for recovery of a fixed-wing uav on a ship using a net carried by multirotor uavs. In *2016 International Conference on Unmanned Aircraft Systems (ICUAS)*, pages 964–973. IEEE, 2016.

[8] Kristian Klausen, Thor I Fossen, and Tor Arne Johansen. Autonomous recovery of a fixed-wing uav using a net suspended by two multirotor uavs. *Journal of Field Robotics*, 35(5):717–731, 2018.

[9] Peter R Thomas, Ujjar Bhandari, Steve Bullock, Thomas S Richardson, and Jonathan L Du Bois. Advances in air to air refuelling. *Progress in Aerospace sciences*, 71:14–35, 2014.

[10] Daniel Briggs Wilson. *Guidance, Navigation and Control for UAV Close Formation Flight and Airborne Docking*. PhD thesis, University of Sydney, 2015.

[11] DARPA. Gremlins program demonstrates airborne recovery. Defense Projects, 05 2021.

[12] Inyeni Amakuro Showers et al. *Development of an autonomous airborne docking and undocking system for micro drones to a mother drone*. PhD thesis, Cape Peninsula University of Technology, 2019.

[13] Kevin Ling. Precision landing of a quadrotor uav on a moving target using low-cost sensors. Master's thesis, University of Waterloo, 2014.

[14] Alexandre Borowczyk, Duc-Tien Nguyen, André Phu-Van Nguyen, Dang Quang Nguyen, David Saussié, and Jerome Le Ny. Autonomous landing of a multirotor micro air vehicle on a high velocity ground vehicle. *Ifac-Papersonline*, 50(1):10488–10494, 2017.

[15] Ewoud JJ Smeur, Qiping Chu, and Guido CHE De Croon. Adaptive incremental nonlinear dynamic inversion for attitude control of micro air vehicles. *Journal of Guidance, Control, and Dynamics*, 39(3):450–461, 2016.

[16] Ewoud JJ Smeur, Guido CHE de Croon, and Qiping Chu. Cascaded incremental nonlinear dynamic inversion for mav disturbance rejection. *Control Engineering Practice*, 73:79–90, 2018.

[17] Muhammad Tahir, Sayed Saad Afzal, Muhammad Saad Chughtai, and Khurram Ali. On the accuracy of inter-vehicular range measurements using gnss observables in a cooperative framework. *IEEE Transactions on Intelligent Transportation Systems*, 20(2):682–691, 2018.

[18] Adam Marut, Konrad Wojtowicz, and Krzysztof Falkowski. Aruco markers pose estimation in uav landing aid system. In *5th International Workshop on Metrology for AeroSpace (MetroAeroSpace)*, pages 261–266. IEEE, 2019.